Additive Manufacturing: Metallurgy, Cut Analysis & Porosity

The latest eBook from Advanced Optical Metrology. Download for free.

12 Advanced Optical Metrology

Additive Manufacturing: Metallurgy, Cut Analysis & Porosity

EVIDENT OLYMPUS

WILEY

In industry, sector after sector is moving away from conventional production methods to additive manufacturing, a technology that has been recommended for substantial research investment.

Download the latest eBook to read about the applications, trends, opportunities, and challenges around this process, and how it has been adapted to different industrial sectors.

EVIDENT OLYMPUS

WILEY

Attractive Electron Delocalization Behavior of FeCoMoPB Amorphous Nanoplates for Highly Efficient Alkaline Water Oxidation

Qianqian Wang, Zhe Jia, Jiaqi Li, Yezeng He, Yiyuan Yang, Yongjie Li, Ligang Sun, and Baolong Shen*

The rational design of high-performance and cost-effective electrocatalysts to overcome the kinetically sluggish water oxidation reaction is a grand challenge in water electrolysis. Transition metals with incompletely filled *d* orbitals are expected to have intrinsic electronic interaction to promote the reaction kinetics, however, the construction of multiple active sites is still a bottleneck problem. Here, inspired by an amorphous alloy design strategy with chemical tunability, a noble-metal-free FeCoMoPB amorphous nanoplate for superior alkaline water oxidation is developed. The achieved overpotentials at current densities of 10, 100, and 500 mA cm^{-2} are 239, 281, and 331 mV, respectively, while retaining a reliable stability of 48 h, outperforming most currently available electrocatalysts. Experimental and theoretical results reveal that the chemical complexity of the amorphous nanoplate leads to the formation of multiple active sites that is able to greatly lower the free energy of the rate-determining step during the water oxidation reaction. Moreover, the Mo element would result in an electron delocalization behavior to promote electron redistribution at its surrounding regions for readily donating and taking electrons. This amorphous alloy design strategy is expected to stimulate the development of more efficient electrocatalysts that is applicable in energy devices, such as metal–air batteries, fuel cells, and water electrolysis.

Q. Wang, Z. Jia, J. Li, Y. Yang, Y. Li, B. Shen
School of Materials Science and Engineering
Jiangsu Key Laboratory for Advanced Metallic Materials
Southeast University
Nanjing 211189, P. R. China
E-mail: blshen@seu.edu.cn

Q. Wang
School of Materials Science and Engineering
Jiangsu Key Laboratory of Advanced Structural Materials and Application Technology
Nanjing Institute of Technology
Nanjing 211167, P. R. China

Y. He
School of Materials Science and Physics
China University of Mining and Technology
Xuzhou 221116, P. R. China

L. Sun
School of Science
Harbin Institute of Technology
Shenzhen 518055, P. R. China

1. Introduction

As society seeks to drastically reduce the future usage of fossil fuels, designing and fabricating novel water splitting electrocatalysts for efficient and reliable hydrogen production is a critically important and challenging research problem.[1] However, the sluggish kinetic of water oxidation reaction (also referred to as oxygen evolution reaction, OER) on anode involving a four-electron transfer process raises a primary obstacle in the water electrolysis reaction.[2] Thus, developing highly efficient and reliable OER electrocatalysts to lower the energy barrier of water electrolysis has been a primary bottleneck challenge. To date, IrO_2 and RuO_2 nanoparticles with high electrocatalytic activity are recognized as the benchmark commercial OER electrocatalysts. Nevertheless, their high cost and resource scarcity greatly restrict the large-scale implementation of the water electrolysis technology. Therefore, it has attracted great research attentions to design novel OER electrocatalysts with low cost, high activity, and strong reliability.

To address these requirements, amorphous alloys with a short-range ordered and long-range disordered atomic structure have exhibited superior performance as catalytic materials compared with their crystalline counterparts.[3] The atoms in the amorphous alloys are thermodynamically unstable and the atomic coordination numbers are typically unsaturated, which is able to provide more active sites for electrochemical reaction.[4] Moreover, amorphous alloys with several intrinsic characteristics including structural heterogeneities,[5] multicomponents,[6] strong corrosion resistance,[7] and so forth, have been largely reported to be promising electrocatalysts for water splitting reactions.[8] Particularly, it was found that the FeCoNiB amorphous nanoparticles exhibit a low overpotential of 274 mV to deliver a current density of 10 mA cm^{-2} for OER reaction in 1.0 M KOH solution.[9] FeNiPBO amorphous nanocages present a superior OER activity (236 mV @ 10 mA cm^{-2}) owing to their synergistic function and unique morphology.[10] Doping W and P elements into FeB amorphous alloy would tune the electronic property and enhance surface reconstruction that extremely promote the OER activity.[11] Thanks to the

ADVANCED
SCIENCE NEWS
www.advancedsciencenews.com

NANO · MICRO
small
www.small-journal.com

honeycombed nanoporous surface structure and lattice distortion effect, NiZrTiPt amorphous ribbon exhibit a low overpotential and Tafel slope in hydrogen evolution reaction (HER).[12] The self-construction behavior of Au-rich interface in AlNiCoMnYAu amorphous ribbon provide a large amount of active site for the enhancement of electrochemical activity.[13] The PdPtCuNiP high-entropy amorphous alloys with a nanosponge structure deliver abundant chemically active sites to achieve a comparable HER activity with Pt/C catalysts.[14] Furthermore, our recent reports found that the coexistence of P and B in FeCoNiPB high-entropy amorphous nanoparticles present a synergistic effect on electron transportation during the OER process, where the P and B act as the electron acceptor and donator, respectively.[15] The structural and chemical heterogeneities of the FeNiPC amorphous alloy display a significant contribution to optimize the rate-determining steps for OER.[16] In addition, the amorphous alloy catalysts have been widely employed as dealloying templates due to their multicomponent nature, such as Pd-Ni-P,[17] Pd-Cu-Ni,[18] and Au-Cu-Si[19] amorphous alloys. The enlarged surface area is also an important factor to promote the reaction of water electrolysis. Nevertheless, it is worthwhile that noble metal alloying is still a mainstream process for developing highly active amorphous alloy electrocatalysts, achieving the goal of rational design of electrocatalysts using low-cost elements is still an ongoing research challenge.

With respect to the compositional selection of the electrocatalysts, great research attention has been paid on to the exploration of transitional metals (i.e., Fe, Co, Ni) to substitute noble metal-based catalysts owing to the intrinsically low conductivity and high electrocatalytic activity.[20] The unfilled d orbitals of the transitional metals enable them easier to gain and lose electrons with variable valence states, which would enhance the electron transfer ability during the electrocatalytic process. Transitional metal Mo with 5 electrons filled in the 4d orbital and 1 electron filled in the 5s orbital is an ideal alloying element to effectively tune electronic structure for electrocatalytic materials.[21] Recent reports have demonstrated significant advances to develop electrocatalysts based on Mo elements. In particular, $NiMo_3S_4$[22] and MoS_2-Ni_3S_2[23] hybrid electrocatalysts have exhibited excellent activity of water electrolysis owing to the Mo active site possessing superior adsorption capability toward hydrogen protons that would be able to promote the sluggish kinetics. While tremendous studies have been dedicated to develop the function of Mo on the promotion of water electrolysis, most of them are based on the binary materials and crystalline structure (i.e., MoS_2) which is in fact limited by their synergistic function of multicomponent. Such limitation motivates the compositional and structural design we developed in this work. Here, we report noble-metal free FeCoMoPB amorphous alloys via a green and facile chemical reduction process that present superior water oxidation activity in the alkaline condition (**Figure 1**a). Various atomic ratios of $(FeCo)_{100-x}$: Mo_x ($x = 0$, 3, 5, 7 and 10, denoted as Mo_0, Mo_3, Mo_5, Mo_7, and Mo_{10}) are initially collected to demonstrate the effect of Mo amount on
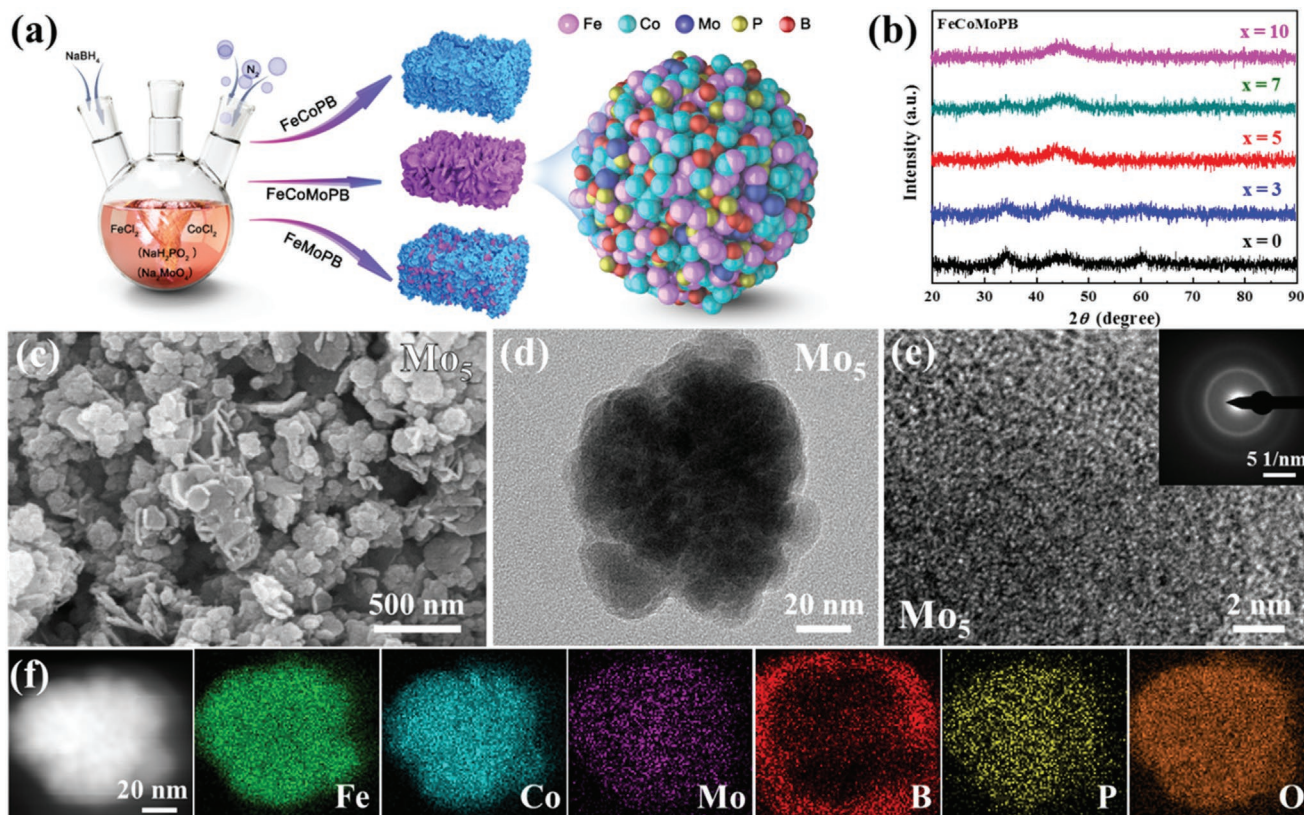
Figure 1. Conceptional design and structural characterization of the FeCoMoPB amorphous alloys. a) Schematic illustration of the preparation process. b) XRD patterns of the prepared samples. c) SEM, d) TEM, and e) HRTEM images of the Mo_5 sample. The inset shows the SAED pattern indicating an amorphous structure. f) Elemental mapping results of the Mo_5 amorphous nanoplates.

**ADVANCED
SCIENCE NEWS**

www.advancedsciencenews.com

**NANO · MICRO
small**

www.small-journal.com

electrocatalytic activity. The Mo_5 amorphous nanoplate requires a low overpotential of 236 mV to achieve the current density of 10 mA cm^{-2} in 1.0 M KOH electrolyte, while maintaining an excellent stability of 48 h, surpassing most of the state-of-the-art non-noble metal-based electrocatalysts. Theoretical simulation suggests that minor addition of Mo element would lead to an electron dislocation behavior which is able to enrich the charge density of the neighboring atoms in FeCoMoPB amorphous nanoplates. Such variation of electronic structure effectively lowers the energy barriers of rate determining steps (RDS) in water oxidation process.

2. Results and Discussion

Figure 1b shows the structural characterization of the as-prepared FeCoMoPB samples. It was found that the X-ray diffraction (XRD) pattern of Mo_0 sample exhibits three diffusive peaks at 33°, 44°, and 61°, respectively (Figure 1b). The peaks at 33° and 61° are corresponding to the formation of metal oxides during the sample preparation and characterization processes under atmospheric exposure, which may lead to an enhanced OER activity under alkaline conditions.[15,24] The broad diffuse diffraction peak at 44° typically indicates an amorphous phase. When the Mo amount is increased from Mo_0 to Mo_7, the metal oxide peaks gradually become invisible and the Mo_{10} sample only presents a broad diffuse diffraction peak, indicating the structure is completely amorphous. Such results suggest that an antioxidation ability is promoted along with increasing Mo amounts into the samples. The scanning electron microscopy (SEM) and transmission electron microscopy (TEM) images in Figure 1c,d show a nanoplate morphology of the Mo_5 sample with an average size of ≈20 nm. Figure 1e and inset present the high-resolution TEM (HRTEM) image and the corresponding selected area electron diffraction (SAED) pattern of the Mo_5 sample. Broad diffuse rings without lattice fringes are observed, corroborating its amorphous structure. Moreover, it is noteworthy that an inhomogeneous contrast with bright and dark regions is clearly observed in Figure 1e, indicating the Mo_5 sample possesses local atomic ordering at sub-nanoscale, which is in great agreement with other reports.[25] The elemental mapping results of Fe, Co, Mo, P, B, and O in the Mo_5 amorphous nanoplate are acquired by the energy-dispersive X-ray spectroscopy (EDX) (Figure 1e). The elements of Fe, Co, Mo, P, and O exhibit uniform distributions in the sample matrix, whereas the B element is enriched at the outer layer of the nanoplates. To investigate the phenomenon of B segregation, we also carried out the microstructural characterization and elemental distribution of the Mo_0 and FeCoMoB samples, as shown in Figures S1 and S2 (Supporting Information). The Mo_0 sample exhibits a wrapped nanofilm morphology with a clear amorphous structure (Figure S1a–c, Supporting Information) and all of the elements are homogeneously distributed (Figure S1d, Supporting Information). With respect to the FeCoMoB sample, the amorphous structure and two typical morphologies including nanofilms and nanoplates are observed (Figure S2a–c, Supporting Information), while the elements are also uniformly distributed (Figure S2d,e, Supporting Information). Such results indicate that the coexistence of Mo and P elements would promote segregation phenomenon of B element,

which is possibly owing to their large negative mixing enthalpy during the synthetic process. The enrichment of B element in the Mo_5 sample would optimize the RDS of OER that will be discussed in the theoretical simulation section.

To determine the effect of Mo addition on chemical valent states, we carried out the X-ray photoelectron spectrometry (XPS) characterization for the elements of Fe, Co, Mo, P, B, and O as shown in **Figure 2**. It is noteworthy that the Fe and Co elements only exhibit oxidized states of Fe^{2+} (709.5 eV), Fe^{3+} (712.8 eV), and Co^{2+} (781.1 eV) on the Mo_0 sample, respectively, whereas Fe^0 (706.5 eV) and Co^0 (777.8 eV) peaks are clearly observed on the Mo_5 sample (Figure 2a,b). The synergistic function of metallic and oxidized states of Fe and Co elements on Mo_5 sample would promote the electron transportation during the four-electron transfer process of the water oxidation, suggesting that it might lead to an enhanced OER activity.[15] The binding energies of Mo 3d can be deconvoluted into two peaks at 232.1 and 235.5 eV, demonstrating Mo^{6+} is the primary specie on the Mo_5 sample (Figure 2c). The peaks of P 2p and B 1s at 133.1 and 191.3 eV on the Mo_0 and Mo_5 samples represent the existence of PO_x and BO_x species, whereas additional M-P (129.5 eV) and M-B (188.2 eV) peaks are observed on the Mo_5 sample, respectively (Figure 2d,e), implying an enhanced electron interaction behavior occurred at the surface of Mo_5 sample.

Figure 3 shows the electrocatalytic performance of the as-prepared FeCoMoPB amorphous alloys in 1.0 M KOH solution. As shown in Figure 3a, the achieved potentials of the Mo_5 sample at the current densities of 10, 100, and 500 mA cm^{-2} are 1.469, 1.511, and 1.561 V, respectively, which are much lower than those of the Mo_0, Mo_3, Mo_7, and Mo_{10} samples as well as the benchmark RuO_2 nanoparticles. The mass activities that are converted from the Linear sweep voltammetry (LSV) curves of the as-prepared samples also present the same trend, that is, the potential of 1.529 V is required for the Mo_5 sample to drive the current density of 1000 mA mg^{-1}, which is much lower than those of the other samples and RuO_2 nanoparticles (Figure 3b). More importantly, the Mo_5 sample only requires 1.552 and 1.571 V to drive large current densities of 2000 and 3000 mA mg^{-1}, respectively, demonstrating its great potential in future industrial application. The resulting OER Tafel slope of the Mo_5 sample is 38 mV dec^{-1}, which is also significantly promoted than those of the other samples and RuO_2 nanoparticles (Figure 3c). To elucidate the effect of P element, we also carried out the OER activity of the FeCoMoB sample as shown in Figure S3 (Supporting Information). The obtained overpotential (@ 10 mA cm^{-2}) and Tafel slope of the FeCoMoB sample are 270 mV and 54 mV dec^{-1}, respectively, which are much higher than those of the Mo_5 amorphous nanoplates. Figure 3d shows the electrochemical impedance spectroscopy (EIS) measurements with the fitting equivalent circuit model of the Nyquist plots (Figure 3d inset) for the as-prepared samples. The R_s and R_{ct} represent the resistance of the electrolyte and the as-prepared samples, respectively. It is well accepted that the value of R_{ct} is correlated to the radius of the semicircles in the Nyquist plots, that is, a smaller semicircle typically indicates a better electron transfer ability for the samples.[26] The Mo_5 amorphous nanoplates present a smallest semicircle diameter compared to those of the other samples, indicating its

**ADVANCED
SCIENCE NEWS**

www.advancedsciencenews.com

**NANO · MICRO
small**

www.small-journal.com
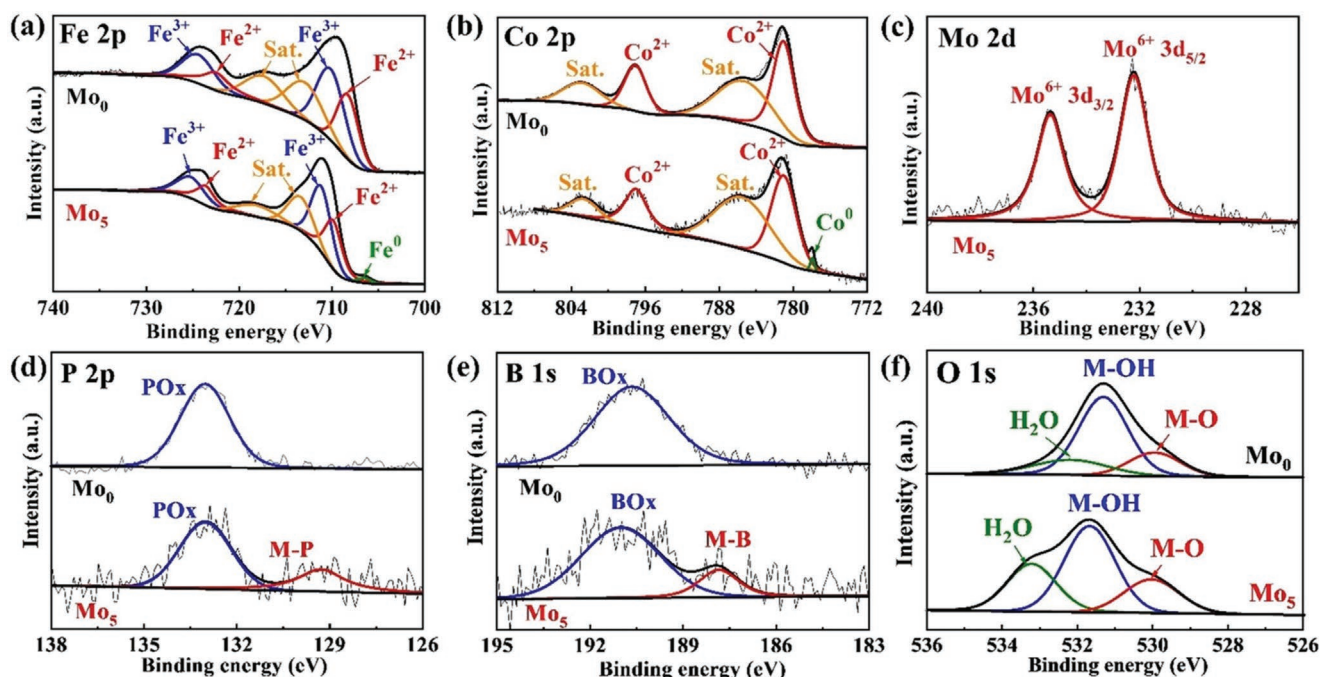
Figure 2. XPS analysis. High-resolution XPS profiles of a) Fe 2p, b) Co 2p, c) Mo 2d, d) P 2p, e) B 1s, and f) O 1s for the Mo_5 amorphous nanoplates.

stronger electron transfer ability during the OER performance. To emphasize the significant contribution of electrochemical surface area (ECSA), we also measured cyclic voltammetry curves of the FeCoMoPB and FeCoMoB amorphous alloys at scan rates ranging at 10–50 mV s^{-1} as shown in Figure 3e; and Figures S4 and S5a (Supporting Information). Accordingly, the double-layer capacitance (C_{dl}) results and ECSA values are obtained in Figure 3f; and Figures S5b and S6 (Supporting Information). It is noteworthy that the ECSA result of the Mo_5 sample exhibits 3.5 and 3.7 times higher than those of the Mo_0 and FeCoMoB samples, whereas the specific surface area of the Mo_5 sample measured by Brunauer–Emmett–Teller (BET) method presents 6.1 times lower than that of the FeCoMoB sample (Figure S7, Supporting Information). Such results suggest that the Mo_5 amorphous nanoplate with more exposed active sites significantly promotes the OER activity. Figure 3g; and Table S1 (Supporting Information) show the OER activity comparison of the Mo_5 amorphous nanoplate with several state-of-the-art noble-meal-free electrocatalysts in 1.0 KOH solution, such as Fe-,[27] Co-,[28] and Ni-based[29] electrocatalysts. The Mo_5 amorphous nanoplate with the overpotential of 239 mV at the current density of 10 mA cm^{-2} locates at the right-top corner, indicating its fabulous OER performance. Furthermore, the Mo_5 amorphous nanoplate also presents a robust OER stability performance over 48 h with a negligible overpotential amplification at the current density of 10 mA cm^{-2} (Figure 3h), outperforming most of the reported electrocatalysts.

To highlight the excellent stability of the Mo_5 amorphous nanoplates, its structural variation after 48 h OER is characterized by TEM (**Figure 4**). Two typical morphologies of the used Mo_5 sample including sheet-like and nanoplate structures are shown in Figure 4a,b, respectively. Figure 4c shows the HRTEM image of the selected area from the nanoplate structure,

demonstrating the structure maintains in amorphous. However, the HRTEM images (Figure 4d,e) with the corresponding SAED pattern (Figure 4f) of the sheet-like structure present an obvious nanocrystallization behavior. Lattice space fringes of 2.45, 2.93, and 2.52 Å, which are in agreement with the (111), (220), and (110) planes of FeOOH crystalline phase, are clearly observed (Figure 4d). Moreover, it was found that the FeOOH and CoOOH nanocrystals with the lattice spacings of 2.47 and 2.37 Å at (011) and (001) planes are enriched at the edge of the sheet-like structure, respectively, which would be regarded as the active sites to retain the long OER stability.[30] The elemental mapping results of Mo, Fe, Co, B, P, and O for the used Mo_5 sample present a similar atomic distribution compared with those of the as-prepared Mo_5 sample, further evidencing its excellent stability (Figure 4g). The high resolution XPS results of the Fe 2p, Co 2p, Mo 3d, O 1s, B 1s, and P 2p for the used Mo_5 sample are shown in Figure S8 (Supporting Information). Compared to the Fe 2p and Co 2p binding energies of the as-prepared Mo_5 sample, the used Mo_5 sample exhibits invisible peaks of Fe^0 and Co^0, while the Co^{3+} peak starts to appear (Figure S8a,b, Supporting Information). These results indicate that the Fe and Co elements are gradually oxidized to higher valence states during the OER testing, which is in agreement with the formation of (Fe, Co)OOH. However, the signals of Mo 3d, B 1s, and P 2p are not detectable for the used Mo_5 sample, which is attributing to the formation of metal hydroxides that would be covering on the sample surface (Figure S8c–g, Supporting Information).

To uncover the origin of the superior water oxidation activity, density functional theory (DFT) simulations of local coordination environment of various active sites are carried out for the Mo_0 and Mo_5 samples (**Figure 5**). Figure 5a; and Figures S9 and S10 (Supporting Information) present the free energy diagrams

ADVANCED
SCIENCE NEWS
www.advancedsciencenews.com

NANO · MICRO
small
www.small-journal.com
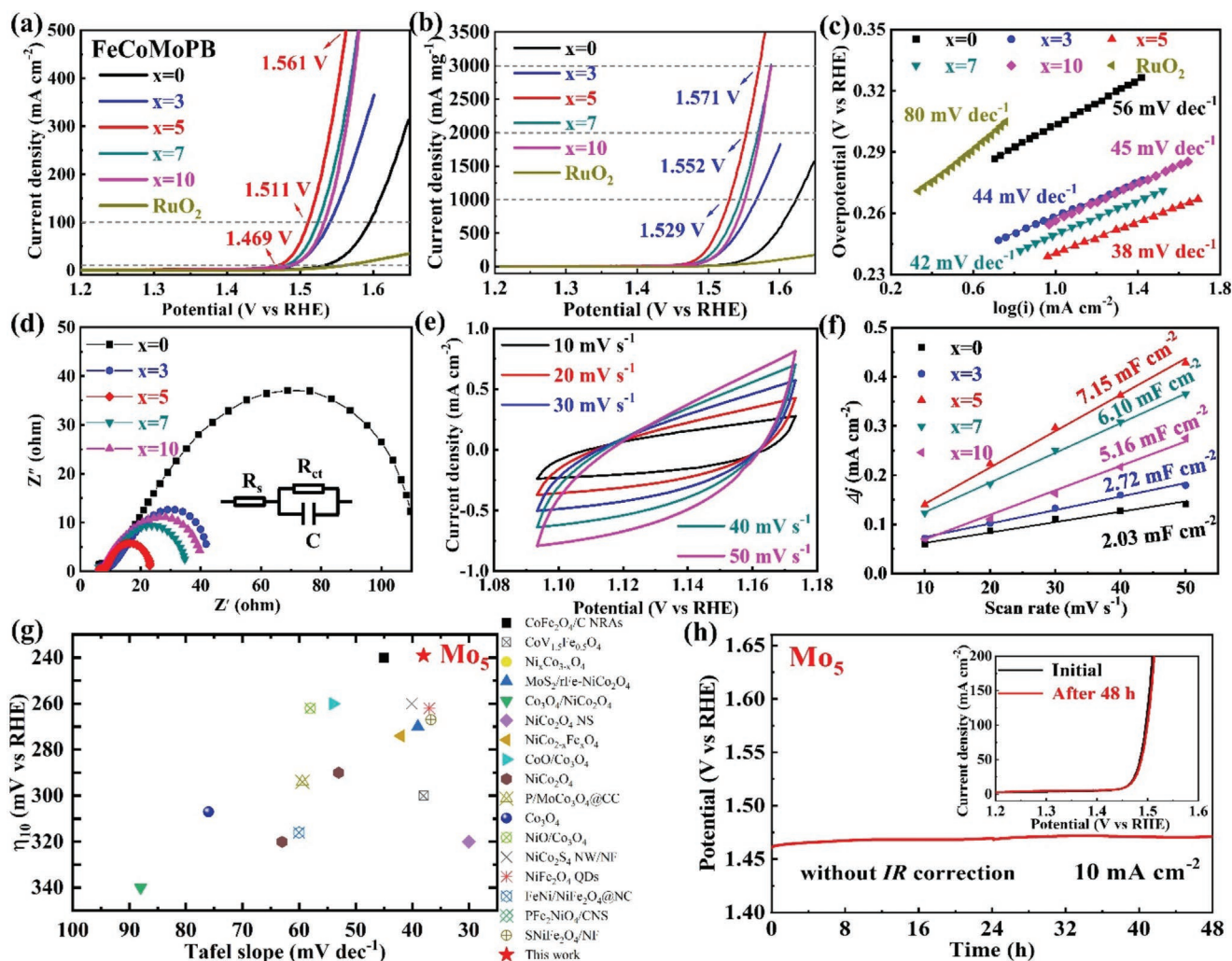
Figure 3. Electrocatalytic performance in 1.0 M KOH solution. a) OER polarization curves, b) mass activity, c) Tafel slopes, d) EIS measurements, e) cyclic voltammetry curves, f) C_{dl} results of the as-prepared FeCoMoPB amorphous alloys. g) Comparison of OER performance with state-of-the-art noble-meal free electrocatalysts. h) Stability test of the Mo_5 amorphous nanoplates at the current density of 10 mA cm^{-2}.

of the water oxidation process of the Mo_0 and Mo_5 samples at the equilibrium potential of 1.23 V. Four representative active sites including FeCo bridge site, B site, FeFeCo/MoFeCo hollow site, and P site are considered in this work. If not specifically mentioned, the active sites are coordinated with first neighboring of Mo atom for the Mo_5 sample. Figure 5a inset shows the adsorption of *OH, *O, and *OOH onto the FeCo bridge site. It is noteworthy that the RDS of the water oxidation process for the FeCo bridge site and P site is the transition from *O to *OOH, whereas the RDS for the B site and FeFeCo/MoFeCo hollow site is the transition from *OOH to O_2, respectively. Particularly, the free energies from *O to *OOH of the FeCo bridge site (Figure 5a) and P site (Figure S10, Supporting Information) for the Mo_5 sample are 1.57 and 1.71 eV, respectively, presenting much lower values than 1.81 and 1.82 eV for the Mo_0 sample. Such result emphasizes the significant contribution of Mo and P elements to optimize the RDS of water oxidation, which is in great agreement with the OER activity obtained in Figure 3. With respect to the B site, it was found that the free energy from *OOH to O_2 is significantly reduced from 4.59 eV of Mo_0

sample to 3.98 eV of Mo_5 sample, evidencing the important function of B enrichment in the Mo_5 sample. However, compared to the FeFeCo hollow site of the Mo_0 sample, the MoFeCo hollow site of the Mo_5 sample only exhibits lower free energies for the reaction steps of *H_2O to *OH and *OH to *O, the free energy of RDS is not severely optimized (Figure S9, Supporting Information). To further verify the electrocatalytic mechanism, we also calculated the d-orbital partial density of states (d-PDOS) to compare the electronic structure variation of the Mo_0 and Mo_5 samples (Figure 5b). The results of d-PDOS indicate that the addition of Mo element in the Mo_5 sample would result in a slight shift of d-band center away from the Fermi level (E_F) compared to that of the Mo_0 sample, suggesting a stronger antibonding ability of electronic states to optimize the free energy of the water oxidation. Figure 5c shows differential charge density diagrams of the Mo_0 and Mo_5 samples with yellow and cyan colors representing accumulation and depletion of electrons, respectively. A strong electron depletion phenomenon around Mo site is observed in the Mo_5 sample, which would lead to a high charge density and strong conductivity in

ADVANCED
SCIENCE NEWS
www.advancedsciencenews.com

NANO · MICRO
small
www.small-journal.com
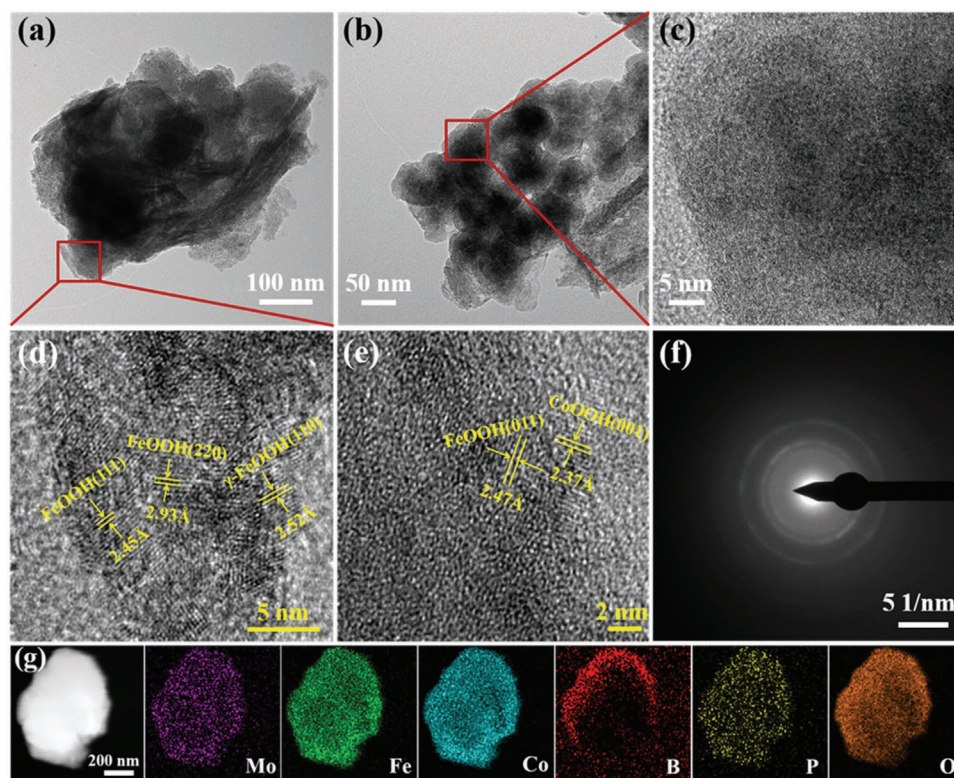
Figure 4. a,b) TEM images, c–e) HRTEM images from the selected areas of a,b,f) SAED pattern, and g) elemental mapping results of the used Mo_5 sample after OER testing for 48 h.

the surrounding area of neighboring atoms. This electron delocalization behavior of Mo atom would be the reason for why the Mo site is not functional to optimize the free energy of RDS for water oxidation (Figure S9, Supporting Information). In comparison, the electrons are preferred to enrich around the neighboring active sites of Mo atom that is able to promote electron transfer ability for lowering the free energy of the RDS. However, too much addition of Mo element, such as Mo_7 and Mo_{10} samples, would give rise to a severe imbalance of charge distribution that is able to deteriorate the OER activity. Hence, the theoretical results demonstrate that the Mo_5 sample would be the most beneficial configuration for the water oxidation activity in this work owing to its appropriate electron delocalization behavior.

3. Conclusion

In this work, noble-metal-free FeCoMoPB amorphous alloys with different Mo amounts have been developed through a facile chemical reduction process for superior water oxidation performance. The Mo_5 sample with an amorphous nanoplate structure exhibits low OER potentials of 1.469, 1.511, and 1.561 V at current densities of 10, 100, and 500 mA cm^{-2}, respectively, while retaining a reliable stability of 48 h in 1.0 M KOH solution, outperforming the performance of Mo_0, Mo_3, Mo_7, and Mo_{10} samples as well as the benchmark RuO_2 nanoparticles. Experimental results and theoretical calculations reveal that the excellent water oxidation activity of the Mo_5 amorphous

nanoplate is originated from an electron delocalization behavior that is able to promote the electron redistribution at the surrounding regions of neighboring active sites. The optimized active sites with an enriched charge density display an essential contribution to lowering the rate-determining step during the oxygen evolution reaction. Our findings deliver a new insight into compositional and structural design of efficient electrocatalysts for widespread applications of water splitting, fuel cell, and metal–air batteries.

4. Experimental Section

Materials Preparation: FeCoMoPB amorphous alloys were synthesized by the previously reported chemical reduction process.[15] Typically, 0.003 mol of mixed metal salts ($Na_2MoO_4\cdot2H_2O$: ($FeCl_2\cdot4H_2O$ and $CoCl_2\cdot6H_2O$) = x : (100–x)) and 0.009 mol of sodium hypophosphite ($NaH_2PO_2\cdot H_2O$) were dissolved in deionized water (x = 0, 3, 5, 7, and 10, denoted as Mo_0, Mo_3, Mo_5, Mo_7, and Mo_{10} for easy identification). Afterward, 0.009 mol of sodium borohydride ($NaBH_4$) was dropwise added into the mixture using a constant-flow pump at a rate of 10 mL min^{-1}. The synthetic process was executed for 50 min under high-purity nitrogen protection with mechanical stirring at room temperature. The resultant precipitates were then washed with deionized water and ethanol in sequence for three times and collected by extraction filtration. All the samples were dried in vacuum at room temperature in 24 h for the subsequent experiments/characterizations. To emphasize the effect of P element, FeCoMoB were also prepared with the same procedure without adding the $NaH_2PO_2\cdot H_2O$.

Structural Characterizations: Structural information of the samples was carried out by XRD (D8-Discover) using Cu Kα radiation (λ = 1.54 Å). SEM (Sirion) and TEM (Tecnai G2 F3) were employed to investigate the
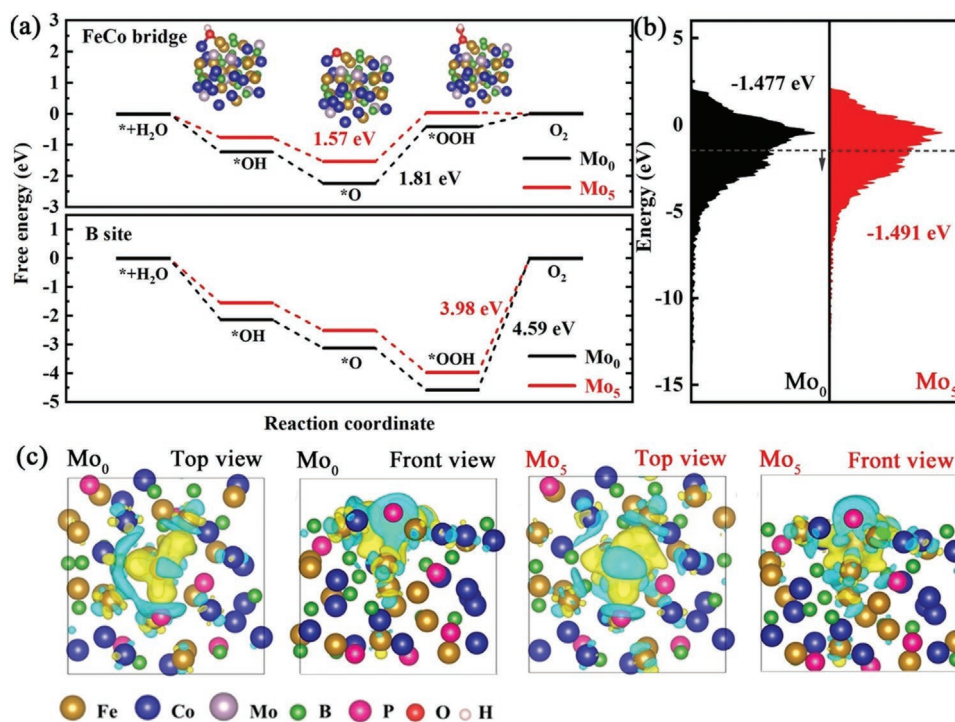
Figure 5. DFT simulations. a) Free energy diagram of the FeCo bridge site and B site for the Mo$_0$ and Mo$_5$ samples at 1.23 V for OER, respectively. The insets show the adsorption of *OH, *O, and *OOH onto the FeCo bridge site with first neighboring of Mo atom. b) d-orbital partial density of states (d-PDOS) and c) differential charge density diagrams of Mo$_0$ and Mo$_5$ samples, yellow and cyan colors represent the accumulation and depletion of electrons, respectively.

surface morphology and spatial structure of the samples. XPS (Thermo Fisher Nexsa) with Al Kα (1486.6 eV) X-ray source was used to measure the surface binding energies of each element. Calibration was carried out using C 1s (284.80 eV) as charge compensation. Specific surface area and pore size distribution were analyzed by N$_2$ absorption and desorption isotherms with the BET method (Autosorb-IQ2). Prior to the N$_2$ adsorption experiment, the sample powders were degassed at 423 K for 2 h.

Electrochemical Measurements: Electrochemical tests were conducted in a standard three-electrode electrochemical workstation (Gamary Interface 1000), whereas a Pt sheet and a standard Hg/HgO electrode were used as the counter electrode and the reference electrode, respectively. For working electrode preparation, catalyst inks were prepared by dispersing powders (5 mg) in a mixture comprising of ethanol (980 µL) and 5% Nafion (20 µL) by ultrasonication for 1 h. Subsequently, 3 µL of ink was uniformly loaded onto a polished glassy carbon electrode (GCE) (0.0707 cm^2) to obtain a loading density of 0.2 mg cm^{-2}. 1.0 M KOH was used as the electrolyte for the OER measurements. The reversible hydrogen electrode (E vs RHE) according to the equation of $E_{RHE} = E_{Hg/HgO} + 0.0591 \times pH + 0.098$ V was used to calibrate the measured potentials. The overpotential (η) was then calculated by the equation of $\eta = E_{versus\ RHE} - 1.23$ V. LSV for OER in this work were measured at a scan rate of 5 mV s^{-1}. The Tafel slope was determined by the linear region of the LSV polarization curves using Tafel equation of $\eta = b \times \log j + a$, where b represents the Tafel slope and j denotes the current density. EIS was recorded at the overpotential of 250 mV in a frequency range from 10 kHz to 0.1 Hz. Chronopotentiometry test was employed to investigate the long-term stability of the electrocatalysts at a constant current density of 10 mA cm^{-2}. Double-layer capacitance (C_{dl}) of the samples was estimated through cyclic voltammetry at different scan rates of 10, 20, 30, 40, and 50 mV s^{-1} in a non-Faradic potential region. ECSA was measured from the double-layer capacitance according to the following equation: ECSA = C_{dl} / C_s.

DFT Calculation: The first-principles calculations were performed in the Vienna Ab-initio simulation package (VASP),[31] using the projector augmented wave (PAW) method.[32] For the FeCoPB amorphous alloy, the structure was built by Ab initio molecular dynamics (AIMD) simulations via a traditional melted and quenched process.[33] In comparison, the FeCoMoPB amorphous slab was constructed by replacing Fe atoms with Mo atoms on the surface of the FeCoPB amorphous alloy. The generalized gradient approximation (GGA) based on Perdew Burke ernzerhof (PBE) parameterization scheme was used to optimize the structures.[34] A 15 Å vacuum layer was constructed to prevent the interaction between the periodic layers. For all surface calculations, the atoms in the bottom layer of the model were fixed and other atoms were allowed to move. The k points of Brillouin zone was set to be 3 × 3 × 1 and the energy cutoff was set to be 500 eV. The force and energy convergence threshold for optimizing configuration were set to be 0.01 eV Å^{-1} and 1 × 10^{-6} eV, respectively. During the OER process, free energies of *OH, *O, and *OOH intermediates were critical for estimating the OER activity, which were calculated based on the equation of $\Delta G = \Delta E_{ads} + \Delta E_{ZPE} + T\Delta ads$, where ΔE_{ads} is the adsorption energy, ΔE_{ZPE} is the zero point energy, T is the surface temperature, and ΔS_{ads} is the corresponding entropy change.

Supporting Information

Supporting Information is available from the Wiley Online Library or from the author.

Acknowledgements

Conflict of Interest

The authors declare no conflict of interest.

Data Availability Statement

The data that support the findings of this study are available from the corresponding author upon reasonable request.

Keywords

[1] a) X. Liu, P. Zou, L. Song, B. Zang, B. Yao, W. Xu, F. Li, J. Schroers, J. Huo, J.-Q. Wang, *ACS Catal.* **2022**, *12*, 3789; b) P. M. Bodhankar, P. B. Sarawade, P. Kumar, A. Vinu, A. P. Kulkarni, C. D. Lokhande, D. S. Dhawale, *Small* **2022**, *18*, 2107572; c) M. Yang, M. Zhao, J. Yuan, J. Luo, J. Zhang, Z. Lu, D. Chen, X. Fu, L. Wang, C. Liu, *Small* **2022**, *18*, 2106554.

[2] a) Z.-J. Chen, T. Zhang, X.-Y. Gao, Y.-J. Huang, X.-H. Qin, Y.-F. Wang, K. Zhao, X. Peng, C. Zhang, L. Liu, M.-H. Zeng, H.-B. Yu, *Adv. Mater.* **2021**, *33*, 2101845; b) L. Zhang, W. Cai, N. Bao, *Adv. Mater.* **2021**, *33*, 2100745; c) Q. Dong, M. Hong, J. Gao, T. Li, M. Cui, S. Li, H. Qiao, A. H. Brozena, Y. Yao, X. Wang, G. Chen, J. Luo, L. Hu, *Small* **2022**, *18*, 2104761.

[3] a) Z. Jia, X. Duan, P. Qin, W. C. Zhang, W. M. Wang, C. Yang, H. Sun, S. Wang, L. C. Zhang, *Adv. Funct. Mater.* **2017**, *27*, 1702258; b) S. X. Liang, Z. Jia, Y. J. Liu, W. C. Zhang, W. M. Wang, J. Lu, L.-C. Zhang, *Adv. Mater.* **2018**, *30*, 1802764; c) Y. Tan, F. Zhu, H. Wang, Y. Tian, A. Hirata, T. Fujita, M. Chen, *Adv. Mater. Interfaces* **2017**, *4*, 1601086.

[4] a) Z. J. Wang, M. X. Li, J. H. Yu, X. B. Ge, Y. H. Liu, W. H. Wang, *Adv. Mater.* **2019**, *32*, 1906384; b) X. Liu, S. Ju, P. Zou, L. Song, W. Xu, J. Huo, J. Yi, G. Wang, J.-Q. Wang, *J. Alloys Compd.* **2021**, *880*, 160548; c) K. Wu, Y. Meng, J. Xu, K. Edalati, H. Shao, W. Li, H.-J. Lin, *Scr. Mater.* **2020**, *188*, 135.

[5] a) J. C. Qiao, Q. Wang, J. M. Pelletier, H. Kato, R. Casalini, D. Crespo, E. Pineda, Y. Yao, Y. Yang, *Prog. Mater. Sci.* **2019**, *104*, 250; b) W. H. Wang, *Prog. Mater. Sci.* **2019**, *106*, 100561.

[6] a) S. Mukherjee, R. C. Sekol, M. Carmo, E. I. Altman, A. D. Taylor, J. Schroers, *Adv. Funct. Mater.* **2013**, *23*, 2708; b) G. Doubek, R. C. Sekol, J. Li, W.-H. Ryu, F. S. Gittleson, S. Nejati, E. Moy, C. Reid, M. Carmo, M. Linardi, P. Bordeenithikasem, E. Kinser, Y. Liu, X. Tong, C. O. Osuji, J. Schroers, S. Mukherjee, A. D. Taylor, *Adv. Mater.* **2016**, *28*, 1940.

[7] a) C. Qin, D. Zheng, Q. Hu, X. Zhang, Z. Wang, Y. Li, J. Zhu, J. Z. Ou, C. Yang, Y. Wang, *Appl. Mater. Today* **2020**, *19*, 100539; b) H. X. Li, Z. C. Lu, S. L. Wang, Y. Wu, Z. P. Lu, *Prog. Mater. Sci.* **2019**, *103*, 235.

[8] a) G. Shao, Q. Wang, F. Miao, J. Li, Y. Li, B. Shen, *Electrochim. Acta* **2021**, *390*, 138815; b) Y. Yan, C. Wang, Z. Huang, J. Fu, Z. Lin, X. Zhang, J. Ma, J. Shen, *J. Mater. Chem. A* **2021**, *9*, 5415.

[9] J. M. V. Nsanzimana, Y. Peng, Y. Y. Xu, L. Thia, C. Wang, B. Y. Xia, X. Wang, *Adv. Energy Mater.* **2018**, *8*, 1701475.

[10] H. Ren, X. Sun, C. Du, J. Zhao, D. Liu, W. Fang, S. Kumar, R. Chua, S. Meng, P. Kidkhunthod, L. Song, S. Li, S. Madhavi, Q. Yan, *ACS Nano* **2019**, *13*, 12969.

[11] Z. Chen, R. Zheng, M. Graś, W. Wei, G. Lota, H. Chen, B.-J. Ni, *Appl. Catal., B: Environ.* **2021**, *288*, 120037.

[12] R. Li, X. Liu, R. Wu, J. Wang, Z. Li, K. C. Chan, H. Wang, Y. Wu, Z. Lu, *Adv. Mater.* **2019**, *31*, 1904989.

[13] S. Ju, J. Feng, P. Zou, W. Xu, S. Wang, W. Gao, H.-J. Qiu, J. Huo, J.-Q. Wang, *J. Mater. Chem. A* **2020**, *8*, 3246.

[14] Z. Jia, K. Nomoto, Q. Wang, C. Kong, L. Sun, L.-C. Zhang, S.-X. Liang, J. Lu, J. J. Kruzic, *Adv. Funct. Mater.* **2021**, *31*, 2101586.

[15] Q. Wang, J. Li, Y. Li, G. Shao, Z. Jia, B. Shen, *Nano Res.* **2022**, *15*, 8751.

[16] Z. Jia, Y. Zhao, Q. Wang, F. Lyu, X. Tian, S.-X. Liang, L.-C. Zhang, J. Luan, Q. Wang, L. Sun, T. Yang, B. Shen, *ACS Appl. Mater. Interfaces* **2022**, *14*, 10288.

[17] J. Yu, Y. Ding, C. Xu, A. Inoue, T. Sakurai, M. Chen, *Chem. Mater.* **2008**, *20*, 4548.

[18] X. Yang, W. Xu, S. Cao, S. Zhu, Y. Liang, Z. Cui, X. Yang, Z. Li, S. Wu, A. Inoue, L. Chen, *Appl. Catal., B: Environ.* **2019**, *246*, 156.

[19] Y. Xu, J. Cheng, P. M. Yiu, G. Shan, T. Shibayama, S. Watanabe, M. Ohnuma, C.-H. Shek, *Nanoscale* **2018**, *10*, 18846.

[20] a) R. Wei, K. Zhang, P. Zhao, Y. An, C. Tang, C. Chen, X. Li, X. Ma, Y. Ma, X. Hao, *Appl. Surf. Sci.* **2021**, *549*, 149327; b) S. Jiang, L. Zhu, Z. Yang, Y. Wang, *Electrochim. Acta* **2021**, *368*, 137618; c) T. N. Huan, N. Ranjbar, G. Rousse, M. Sougrati, A. Zitolo, V. Mougel, F. Jaouen, M. Fontecave, *ACS Catal.* **2017**, *7*, 1520.

[21] P. Y. Kuang, T. Tong, K. Fan, J. G. Yu, *ACS Catal.* **2017**, *7*, 6179.

[22] J. Jiang, M. Gao, W. Sheng, Y. Yan, *Angew. Chem., Int. Ed.* **2016**, *55*, 15240.

[23] Y. Yang, K. Zhang, H. Lin, X. Li, H. C. Chan, L. Yang, Q. Gao, *ACS Catal.* **2017**, *7*, 2357.

[24] a) H. Chen, S. Ouyang, M. Zhao, Y. Li, J. Ye, *ACS Appl. Mater. Interfaces* **2017**, *9*, 40333; b) J. M. V. Nsanzimana, R. Dangol, V. Reddu, S. Duo, Y. Peng, K. N. Dinh, Z. Huang, Q. Yan, X. Wang, *ACS Appl. Mater. Interfaces* **2019**, *11*, 846.

[25] a) Y. H. Liu, D. Wang, K. Nakajima, W. Zhang, A. Hirata, T. Nishi, A. Inoue, M. W. Chen, *Phys. Rev. Lett.* **2011**, *106*, 125504; b) F. Zhu, S. Song, K. M. Reddy, A. Hirata, M. Chen, *Nat. Commun.* **2018**, *9*, 3965; c) Z. Jia, Y. Yang, Q. Wang, C. Kong, Y. Yao, Q. Wang, L. Sun, B. Shen, J. J. Kruzic, *ACS Mater. Lett.* **2022**, *4*, 1389.

[26] Z. Jia, T. Yang, L. Sun, Y. Zhao, W. Li, J. Luan, F. Lyu, L. C. Zhang, J. J. Kruzic, J. J. Kai, J. C. Huang, J. Lu, C. T. Liu, *Adv. Mater.* **2020**, *32*, 2000385.

[27] Z. Liu, B. Tang, X. Gu, H. Liu, L. Feng, *Chem. Eng. J.* **2020**, *395*, 125170.

[28] a) X.-F. Lu, L.-F. Gu, J.-W. Wang, J.-X. Wu, P.-Q. Liao, G.-R. Li, *Adv. Mater.* **2017**, *29*, 1604437; b) K. Chakrapani, G. Bendt, H. Hajiyani, T. Lunkenbein, M. T. Greiner, L. Masliuk, S. Salamon, J. Landers, R. Schlögl, H. Wende, R. Pentcheva, R. Schulz, M. Behrens, *ACS Catal.* **2018**, *8*, 1259; c) H. Hu, B. Guan, B. Xia, X. W. Lou, *J. Am. Chem. Soc.* **2015**, *137*, 5590.

[29] a) Y. Li, P. Hasin, Y. Wu, *Adv. Mater.* **2010**, *22*, 1926; b) J. Bao, X. Zhang, B. Fan, J. Zhang, M. Zhou, W. Yang, X. Hu, H. Wang, B. Pan, Y. Xie, *Angew. Chem., Int. Ed.* **2015**, *54*, 7399; c) Y. Huang, S. L. Zhang, X. F. Lu, Z.-P. Wu, D. Luan, X. W. Lou, *Angew. Chem., Int. Ed.* **2021**, *60*, 11841.

[30] a) J.-X. Feng, H. Xu, Y.-T. Dong, S.-H. Ye, Y.-X. Tong, G.-R. Li, *Angew. Chem., Int. Ed.* **2016**, *55*, 3694; b) J. Zhou, Y. Wang, X. Su, S. Gu,

R. Liu, Y. Huang, S. Yan, J. Li, S. Zhang, *Energy Environ. Sci.* **2019**, *12*, 739; c) W. H. Lee, M. H. Han, Y.-J. Ko, B. K. Min, K. H. Chae, H.-S. Oh, *Nat. Commun.* **2022**, *13*, 605.

[31] G. Kresse, J. Furthmüller, *Phys. Rev. B* **1996**, *54*, 11169.

[32] P. E. Blöchl, *Phys. Rev. B* **1994**, *50*, 17953.

[33] H. Wang, R. Wei, X. Li, X. Ma, X. Hao, G. Guan, *J. Mater. Sci. Technol.* **2021**, *68*, 191.

[34] J. P. Perdew, K. Burke, M. Ernzerhof, *Phys. Rev. Lett.* **1996**, *77*, 3865.